AGU PUBLICATIONS

JGR

Journal of Geophysical Research: Space Physics

RESEARCH ARTICLE

10.1002/2014JA020129

Key Points:
- ULF waves nominally make small contributions to global Joule heating
- Contributions to global heating are significant in extreme events
- ULF waves nominally make important contributions to local Joule heating

Supporting Information:
- Readme
- Figure S1
- Figure S2

Correspondence to:
M. D. Hartinger,
mdhartin@umich.edu

Citation:
Hartinger, M. D., M. B. Moldwin, S. Zou, J. W. Bonnell, and V. Angelopoulos (2015), ULF wave electromagnetic energy flux into the ionosphere: Joule heating implications, *J. Geophys. Res. Space Physics*, *120*, 494–510, doi:10.1002/2014JA020129.

Received 25 APR 2014
Accepted 25 DEC 2014
Accepted article online 6 JAN 2015
Published online 29 JAN 2015

ULF wave electromagnetic energy flux into the ionosphere: Joule heating implications

M. D. Hartinger[1], M. B. Moldwin[1], S. Zou[1], J. W. Bonnell[2], and V. Angelopoulos[3]

[1]Department of Atmospheric, Oceanic, and Space Sciences, University of Michigan, Ann Arbor, Michigan, USA, [2]Space Science Laboratory, University of California, Berkeley, California, USA, [3]Department of Earth and Space Sciences, University of California, Los Angeles, California, USA

Abstract Ultralow-frequency (ULF) waves—in particular, Alfvén waves–transfer energy into the Earth's ionosphere via Joule heating, but it is unclear how much they contribute to global and local heating rates relative to other energy sources. In this study we use Time History of Events and Macroscale Interactions during Substorms satellite data to investigate the spatial, frequency, and geomagnetic activity dependence of the ULF wave Poynting vector (electromagnetic energy flux) mapped to the ionosphere. We use these measurements to estimate Joule heating rates, covering latitudes at or below the nominal auroral oval and below the open/closed field line boundary. We find ULF wave Joule heating rates (integrated over 3–30 mHz frequency band) typically range from 0.001 to 1 mW/m^2. We compare these rates to empirical models of Joule heating associated with large-scale, static (on ULF wave timescales) current systems, finding that ULF waves nominally contribute little to the global, integrated Joule heating rate. However, there are extreme cases with ULF wave Joule heating rates of $\geq$10 mW/m^2—in these cases, which are more likely to occur when $Kp \geq 3$, ULF waves make significant contributions to the global Joule heating rate. We also find ULF waves routinely make significant contributions to local Joule heating rates near the noon and midnight local time sectors, where static current systems nominally contribute less to Joule heating; the most important contributions come from lower frequency (<7 mHz) waves.

1. Introduction

1.1. ULF Waves and Their Ionospheric Impacts

Ultralow-frequency (ULF) waves can play prominent roles in the dynamics of the Earth's ionosphere. In at least some cases, the amount of energy ULF waves release is an appreciable fraction (as much as 30%) of the energy released during a substorm [*Greenwald and Walker*, 1980; *Rae et al.*, 2007]. These waves are a source of electric field variability in the ionosphere, which is an important contribution to the overall Joule heating rate [*Codrescu et al.*, 1995]. Several studies demonstrated that ULF waves can provide a substantial energy input to the ionosphere via Joule heating [e.g., *Crowley et al.*, 1985; *Lathuillere et al.*, 1986; *Rae et al.*, 2007]; for example, *Crowley et al.* [1985] measured ionosphere ion temperature variations associated with ULF wave-induced Joule heating that were comparable to the ambient temperature. Through their effect on the ionosphere, ULF waves can indirectly affect space weather. For example, ULF electric field perturbations in the ionosphere cause Joule heating, which in turn affects the temperature of the ionosphere and neutral atmosphere and can lead to thermosphere expansion and then enhanced satellite drag [*Dessler*, 1959a; *Fuller-Rowell et al.*, 1994].

The term "ULF wave," in the context of magnetospheric plasma waves, includes waves with frequencies as high as 5 Hz [*Jacobs et al.*, 1964]. In the present study, we are only concerned with frequencies in the spacecraft frame of 3–30 mHz (33–333 s periods). The large-scale dynamics and structure of these waves are typically captured by ideal magnetohydrodynamics (MHD). In the limit of cold plasma and a uniform medium, ideal MHD predicts two propagating wave modes: shear Alfvén waves and fast (magnetosonic) mode waves. Shear Alfvén waves only transfer energy along the background magnetic field direction, whereas fast mode waves can transfer energy in all directions [*Kivelson and Russell*, 1995, chapter 11].

In the bounded medium of the Earth's magnetosphere, standing Alfvén waves are generated when the northern and southern ionospheres act to reflect and trap Alfvén wave energy in closed field line regions; this trapping leads to standing waves with frequencies related to the Alfvén wave transit time between the two ionosphere boundaries [*Dungey*, 1967]. The lowest frequencies for these standing waves are a few

millihertz in the dayside magnetosphere [*Singer et al.*, 1981]. There are no perfectly standing Alfvén waves since wave energy incident on the ionosphere is only partially reflected, with the amount of reflection depending on the ionospheric conductivity. For example, roughly 97% of Alfvén wave energy is reflected from the ionosphere for typical dayside conductivities, whereas only 40% is reflected for typical nightside conductivities [*Hughes and Southwood*, 1976].

Standing Alfvén waves create a current that closes in the resistive medium of the Earth's ionosphere that gradually dissipates via Joule heating. Due to Joule heating, these waves gradually damp over many wave cycles as they heat the ionosphere/neutral atmosphere [*Newton et al.*, 1978]. Standing Alfvén waves are of particular interest for the present study for two main reasons: (1) they preferentially transfer energy along the magnetic field and into the ionosphere via Joule heating (much more so than ULF wave modes that are not guided by the magnetic field) and (2) they are the most frequently observed type of coherent (i.e., not noise) ULF wave activity in the 3–30 mHz frequency range [*Anderson et al.*, 1990]. For these reasons, standing Alfvén waves ought to be the most important ULF wave mode for Joule heating at these frequencies.

Despite case study evidence that ULF waves—in particular, standing Alfvén waves—cause substantial heating in the ionosphere, there is still uncertainty whether this is a routine occurrence. *Dessler* [1959b] predicted that ULF waves have little effect on overall heating rates/ionosphere temperatures except during geomagnetic storms. *Greenwald and Walker* [1980] noted that *Dessler*'s [1959b] calculation was based on an assumption of high-frequency (1 Hz) waves, and they showed that lower frequency ULF waves can have dissipation rates roughly 2 orders of magnitude larger than those predicted by *Dessler* [1959b]. As noted by *Rae et al.* [2007], there have been few studies quantifying ULF wave energy input to the ionosphere due to observational difficulties; to our knowledge, there have been no attempts to statistically quantify nominal ULF wave Joule heating rates for different frequencies, spatial regions, and geomagnetic activity levels.

1.2. Measuring AC (ULF) and DC Ionospheric Energy Deposition Rates

Previous studies have used satellite data to map electromagnetic energy fluxes, or the Poynting vector (**S**), from the magnetosphere to the ionosphere. Using these observations, they have quantified the electromagnetic energy input (or output) in different spatial regions, for different frequency ranges, and for different levels of geomagnetic activity [e.g., *Gary et al.*, 1995; *Angelopoulos et al.*, 2002; *Keiling et al.*, 2003; *Rae et al.*, 2007; *Hartinger et al.*, 2011]. Two different setups for these observations are shown in Figure 1: mapping the parallel (to magnetic field) Poynting vector ($S_{\|}$) from a satellite in low Earth orbit (LEO, apogee <2000 km) and mapping $S_{\|}$ from a satellite in a low inclination, high Earth orbit (HEO, apogee outside geostationary orbit) with apogee near 13 R_E (representing a Time History of Events and Macroscale Interactions during Substorms, or THEMIS, satellite). In either case, the field lines are assumed to be equipotential with no energy loss along a field line so that $S_{\|}$ is scaled by the cross-sectional area of a flux tube [e.g., *Rae et al.*, 2007]

$$S_{\|i} = S_{\|o} \times \frac{|B_i|}{|B_o|} \tag{1}$$

where $S_{\|i}$ is the parallel Poynting vector at the ionosphere, $S_{\|o}$ is at the observation point, and $|B_i|$ and $|B_o|$ are the magnetic field strengths at the ionosphere and observation point, respectively.

These two types of satellite observations are similar in many ways. Since they measure $S_{\|o}$ in situ, they need not rely on assumptions/additional measurements required for estimates of $S_{\|i}$ using ground-based observations, such as measurements of the Pedersen conductivity. In the context of ULF waves, however, there is an important difference between satellite observations of $S_{\|o}$ at LEO versus higher apogee orbits. LEO probes move rapidly through ULF wave structures introducing frequency shifts as well as time-space ambiguities [*Anderson et al.*, 1989; *Le et al.*, 2011]. In contrast, probes with higher apogee orbits (e.g., THEMIS and Polar) are well suited for studying the frequency dependence of ULF wave energy transfer. Their slow motion near apogee combined with large (compared to LEO) wave spatial scales allows them to linger for longer periods in localized ULF wave structures, provided the bulk flow perpendicular to the magnetic field is not large (as indicated by, for example, the results of *Dombeck et al.* [2005], *Rae et al.* [2007] and *Hartinger et al.* [2011]). This allows them to sample a single-wave frequency over many wave cycles, separate AC from DC variations, and compare the AC/ULF contribution to $S_{\|}$ (separate from, for example, contributions from large-scale currents that are static on ULF wave timescales) directly with observations of Joule heating. This is illustrated in Figure 1a; here distorted magnetic field lines are colored according to the

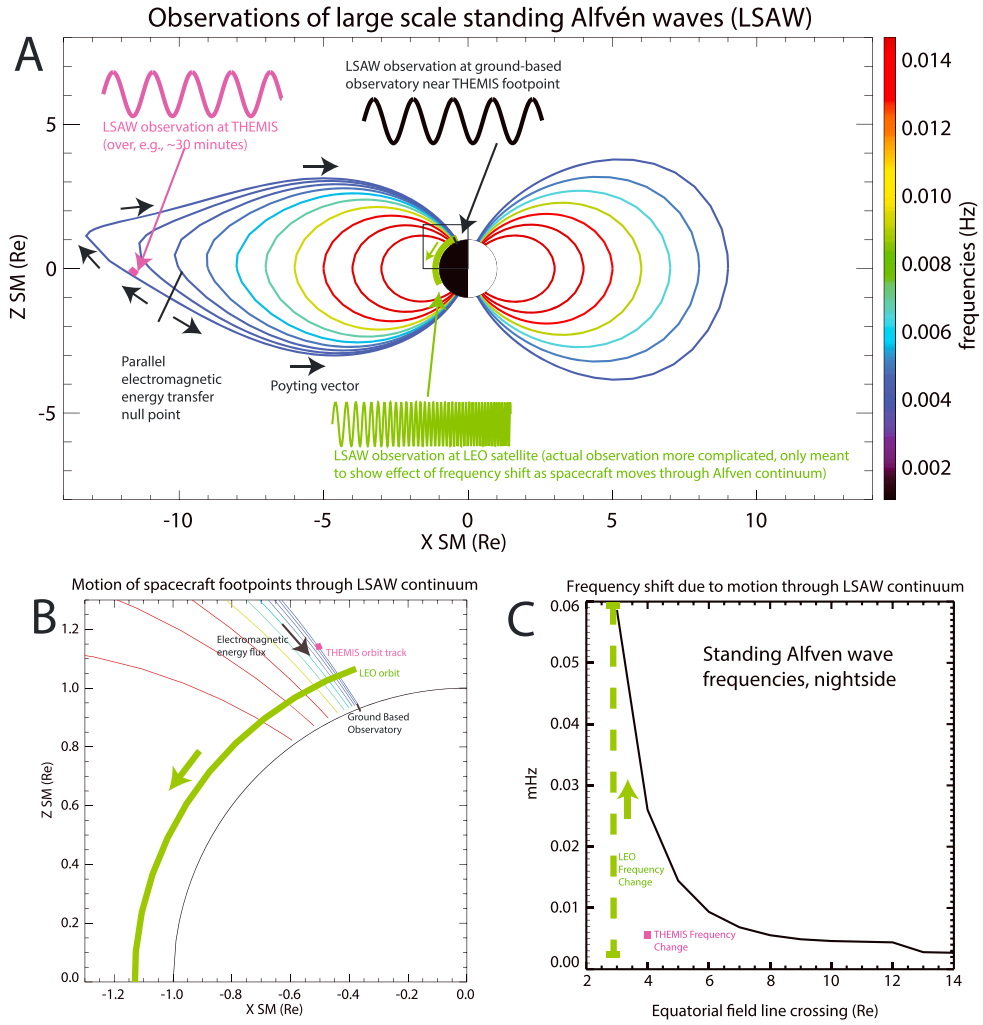

Figure 1. (a) Magnetic field lines are shown from the T89 model, where color indicates the standing Alfvén wave frequency. Typical orbit tracks for a half-hour period are shown for a THEMIS (pink) and LEO (green) satellite. (b) Zooming in on the gray box in Figure 1a, the distance in *L* covered by THEMIS is much smaller than for the LEO satellite. (c) Due to the LEO satellite's rapid transit of wave spatial structures (compared to THEMIS), it experiences a substantial frequency shift as it moves through a continuum of standing Alfvén wave frequencies.

local standing Alfvén wave frequency. A THEMIS probe moves slowly through the continuum of standing waves (pink line), sampling the electromagnetic energy flux (black arrows) bound for the ionosphere where it will be lost via Joule heating in the ionosphere (assuming an ideal MHD description, as discussed in section 3.5). There are no significant frequency shifts between wave perturbations observed in situ and on the ground. In contrast, as shown in Figure 1b and 1c, a LEO probe moves much larger distances relative to the local length scale for ULF wave frequency variations (perpendicular wavelength is on the order of 100 km in the north-south direction in the ionosphere compared to roughly 0.1–0.5 R_E near the equatorial plane [*Mann*, 1995, 1997]) on the same timescale (30 min, $\geq$5 ULF wave periods), introducing time-space ambiguities (i.e., one cannot discriminate between wave spatial structures and time variations without additional observations or modeling, as demonstrated by *Le et al.* [2011]) and large frequency shifts due to motion through a continuum of standing Alfvén waves with different frequencies. The focus of this study will be on HEO observations, as our main goal is to examine ULF wave Joule heating contributions.

There are a few approaches used to estimate $S_{\|i}$, depending on satellite orbit and science objectives. In particular, some studies focus on steady or "DC" $S_{\|}$, whereas others focus on the contribution of higher frequency, or "AC" variations to $S_{\|}$. Complicating matters, the definition of "DC" and "AC" can change depending on the phenomena of interest or frame of reference: what is "DC" in one study may be "AC" in

another study. In this study, we define "DC" as static fields or perturbations in the THEMIS satellite frame with frequencies less than 3 mHz, and "AC" as perturbations in the satellite frame with frequencies greater than 3 mHz. We chose this AC/DC division to better understand the role standing Alfvén waves play in Joule heating, since 3 mHz is close to the lower frequency cutoff for standing Alfvén wave activity in the magnetosphere [*Singer et al.*, 1981]. As discussed in the previous section, these waves are expected to make the largest contributions to Joule heating when compared to other ULF wave modes.

1.3. Previous Studies of Ionospheric Energy Deposition Rates

Several studies have used LEO satellites to measure $S_{\parallel}$ and map it to the ionosphere, quantifying electromagnetic energy input. Both *Gary et al.* [1995] and *Olsson et al.* [2004] statistically examined DC electromagnetic energy flux at invariant latitudes (Λ) greater than 40°, finding typical $S_{\parallel}$ values of 1–10 mW/m^2. *Knipp et al.* [2011] also statistically examined DC $S_{\parallel}$, finding similar values in most conditions but substantially larger values (> 100 mW/m^2) during periods of strong east-west interplanetary magnetic field (IMF). Medium Earth orbit satellites have also been used in several studies of $S_{\parallel}$. For example, *Strangeway et al.* [2005] used the Fast Auroral Snapshot Explorer (FAST) satellite to measure $S_{\parallel}$ in the dayside region $60 < \Lambda < 80$, finding values of roughly 0.1–10 mW/m^2 at 4000 km altitude; mapped to the ionosphere, these become roughly 1–100 mW/m^2. *Cosgrove et al.* [2014] constructed an empirical model of Poynting flux based on FAST data, with typical ionospheric model values of 1–10 mW/m^2 for $\Lambda > 60$.

Moving outward, a number of studies have used satellites in higher apogee orbits to measure $S_{\parallel}$ and map it into the ionosphere by assuming no energy is lost as it flows along the magnetic field toward the ionosphere. *Wygant et al.* [2002] observed an event with both large- and small-scale Alfvén wave structures in the plasma sheet boundary layer (PSBL); **S** associated with the large-scale Alfvén wave was roughly 100 mW/m^2 when mapped to the ionosphere (100 km) compared to 4 mW/m^2 for the DC **S** (the latter was associated with convection/field-aligned currents). *Angelopoulos et al.* [2002] observed a dispersive Alfvén wave event in the plasma sheet (PS) with a range of frequencies (1 to 100 mHz) during a geomagnetic substorm, finding maximum mapped Poynting vectors from 31 to 640 mW/m^2 depending on the position of original observation along the field line. *Keiling et al.* [2002, 2003] showed that $S_{\parallel}$ associated with Alfvén waves (frequencies above 5.5 mHz in spacecraft frame) in the PSBL ranges from 0.1 to 125 mW/m^2 when mapped to the ionosphere (~100 km, $\Lambda > 60$) and can provide sufficient energy to generate aurora. *Chaston et al.* [2005] showed with a case study that Alfvén waves in the low-latitude boundary layer ($70 < \Lambda < 80$) with a continuous range of frequencies (1 to 50 mHz, spacecraft frame) would deposit $S_{\parallel}$ in the ionosphere on the order of 1 mW/m^2; similarly, *Dombeck et al.* [2005] showed with a case study that Alfvén waves with frequencies from 0.005 to 4 Hz would deposit $S_{\parallel}$ on the order of 2 mW/m^2 in the ionosphere ($66 < \Lambda < 72$), with most of the energy coming from the lowest-frequency waves. *Janhunen et al.* [2005] examined locations conjugate to the auroral oval and both open/closed field line regions, finding DC and AC Joule heating rates of roughly 1–7 and 0.1–1 mW/m^2, respectively. *Rae et al.* [2007] and *Hartinger et al.* [2011] both observed standing Alfvén waves generated by field line resonance, finding that $S_{\parallel}$ in the ionosphere was roughly 0.4–0.46 and 0.7 mW/m^2, respectively.

1.4. Overview and Goals of This Study

Table 1 summarizes the results of previous satellite observations and estimates of $S_{\parallel i}$. In the present study we shall expand the results in this table by statistically estimating ULF wave (AC, frequency >3 mHz) electromagnetic energy flux as a function of frequency, spatial region, and geomagnetic activity using measurements ($S_{\parallel o}$) from HEO and equation (1). Our goal is to estimate nominal ULF wave Joule heating rates and quantify the contribution of ULF waves to the overall (DC plus AC) Joule heating rate. Our observations simultaneously cover a wide frequency range and spatial region with 5 years of data, expanding previous studies of ULF wave-induced Joule heating and allowing us to test the prediction of *Dessler* [1959b] that this heating is usually negligible. In sections 2 and 3, we describe the instruments, techniques, and assumptions necessary to estimate the electromagnetic energy flux and Joule heating rates. In section 4, we quantify electromagnetic energy flux as a function of frequency, spatial region, and geomagnetic activity level. In section 5, we discuss the implications of ULF wave energy deposition rates for ionospheric Joule heating. Finally, we summarize our results in section 6.

Table 1. Typical Values for DC and ULF $S_{||i}$ Observations From Satellites

	Satellite	Invariant Lat	Frequency	$S_{||}$ (mW/m^2)
Gary et al. [1995]	DE 2	$\Lambda > 40$	Mix[a]	1–10
Olsson et al. [2004]	Astrid 2	$\Lambda > 40$	Mix	1–10
Strangeway et al. [2005]	FAST	$80 > \Lambda > 60$	Mix	1–100
Knipp et al. [2011]	DMSP 15	$\Lambda > 50$	Mix	1 to >100
Cosgrove et al. [2014]	FAST	$\Lambda > 60$	Mix	~1–10
Angelopoulos et al. [2002]	Polar/Geotail	PS	ULF	31–640
Keiling et al. [2002, 2003]	Polar	$\Lambda > 60$	>5.5 mHz	0.1–125
Wygant et al. [2002]	Polar	PSBL	DC/ULF	4 (DC),100 (ULF)
Chaston et al. [2005]	Cluster/FAST	$70 > \Lambda > 80$	1–50 mHz	1
Dombeck et al. [2005]	Polar/FAST	$72 > \Lambda > 66$	0.005–4 Hz	2
Janhunen et al. [2005]	Polar/Astrid 2	$74 > \Lambda > 64$	DC/ULF	1–7 (DC),0.1–1 (ULF)
Rae et al. [2007]	Polar	$76.5 > \Lambda > 66.5$	1.5 mHz	0.4–0.46
Hartinger et al. [2011]	THEMIS	$71.5 > \Lambda > 70.5$	5 mHz	0.7
Present study	THEMIS	$80 > \Lambda > 60$[b]	3–30 mHz	0.001–1

[a]"Mix" means the study did not specifically discriminate between DC and ULF fields.
[b]The present study only includes closed field line regions.

2. Instrumentation

Measurements of the ULF wave **S** used in this study are from the fluxgate magnetometer (FGM) [*Auster et al.*, 2008] and electric field instrument (EFI) [*Bonnell et al.*, 2008] from the five probe THEMIS mission [*Sibeck and Angelopoulos*, 2008]. As in *Hartinger et al.* [2013], only three probes are used for this study: THA, THD, and THE. The probes have perigee and apogee radii of 1.5 R_E and 10–13 R_E, respectively, and inclinations that range from 5 to 12° [*Frey et al.*, 2008]. The satellite spin period is roughly 3 s; we use data sampled at the spin period almost exclusively for this study (with the exception of diagnostics performed on EFI data in the spinning frame). We also use particle data from the ion and electron electrostatic analyzer (ESA) [*McFadden et al.*, 2008] and solid state telescopes (SST) [e.g., *Turner et al.*, 2012] to locate the satellite in different regions (i.e., inside of the magnetosphere/magnetosheath); three-dimensional particle distributions and moments are available at the spin period using both ESA (electrons: 5 eV–30 keV, ions 5 eV–25 keV) and SST (energies above 25 keV). Finally, we obtain geomagnetic activity indices from the Space Physics Data Facility (a project of NASA's Goddard Space Flight Center) OMNIWeb interface at http://omniweb.gsfc.nasa.gov.

3. Methodology

3.1. Data Preparation, Reduction, and Coverage

The database and most of the data processing and reduction procedures used in this study are very similar to *Hartinger et al.* [2013]. For brevity, we only summarize these procedures here, highlighting a few differences between the procedures and data used in *Hartinger et al.* [2013] and those used in the present study.

As in *Hartinger et al.* [2013], we obtained EFI, FGM, ESA, and SST data from the THEMIS website (http://themis.ssl.berkeley.edu/index.shtml), applying calibrations and corrections using the TDAS software package distributed by the THEMIS science team (version 2013-09-12, *Hartinger et al.* [2013] used version 2013-01-07, but there are no important differences between these two versions in the context of Poynting vector measurements). We also use field line tracing routines and magnetic field models from the Geopack library, provided as part of TDAS. We analyzed data from the period 1 February 2008 to 31 July 2013 for THEMIS spacecraft E (THE) and D (THD), and 1 February 2008 to 1 May 2013 for THEMIS spacecraft A (THA, limited interval due to EFI contamination that occurred after 1 May 2013); this extends the *Hartinger et al.* [2013] database forward in time from 1 December 2012. We only used data from THEMIS probes THA, THD, and THE, since they spent the most time in the magnetosphere during this period. We exclusively use fast survey mode data for wave analysis.

EFI measures ULF fluctuations most reliably in the spin plane; we use the approximation $\mathbf{E} \cdot \mathbf{B} = 0$, where **E** is for the electric field and **B** is for the magnetic field, to get the component of the electric field vector along the spin axis (see third to last paragraph of this section for further discussion of this technique's caveats). Spikes, gaps, and step-like changes are removed from the electric and magnetic field 3 s (spin fit) data, and

Table 2. Data Reduction and Total Data Coverage in Days for THA, THD, and THE[a]

	THA	THD	THE
All data	1916	2130	2130
Fast survey	979	1138	1178
In magnetosphere	796	987	1001
Interval > 60 min	876	875	865
Useable FFT data (E/B finite, no spikes, edges removed)	483	579	572
$\vec{E} \times \vec{B} = 0$ (spin axis B is large)	238	301	301
|Sun angle| > 1.75	210	253	253

[a]One day is equivalent to 56.25 samples (nonoverlapping FFT windows).

these data are high pass filtered (frequency > 2 mHz) and rotated into a field-aligned (FA) coordinate system in which *z* is along the background magnetic field, *y* points eastward, and *x* completes the right-hand orthogonal set (pointing radially outward at the equator). The time-averaged Poynting vector is computed using the following expression:

$$\mathbf{S}(f) = \frac{1}{2\mu_0} Re(\mathbf{E}(f) \times \mathbf{B}^*(f)) \tag{2}$$

where f is the frequency, $\mathbf{S}(f)$ is the frequency-dependent Poynting vector in W/m^2, $\mathbf{B}(f)$ and $\mathbf{E}(f)$ are the complex Fourier coefficients for the magnetic and electric fields, respectively, the asterisk indicates the complex conjugate, *Re* indicates the real part of the result, and μ_0 is the permeability of free space. To use this expression, we first calculate complex Fourier coefficients for each vector using a 512 point, 25.6 min discrete Fast Fourier Transform (FFT) window with no overlap between windows. These Fourier coefficients are then used calculate the frequency-dependent **S** as in *Hartinger et al.* [2013].

Equation (2) captures the time average of the Poynting vector at a given frequency, and $\mathbf{S}(f)$ is an indicator of net energy transfer over the course of the FFT window. As discussed by *Keiling* [2009], the time-averaged Poynting vector computed using the perturbation electric and perturbation magnetic fields (whether frequency or time domain) is the relevant quantity for examining net energy transport associated with ULF waves. There are other contributions to the instantaneous Poynting vector—for example, the term that includes the perturbation electric field and background magnetic field, which corresponds physically to the convective transport of electromagnetic energy flux perpendicular to the background field—but they average to zero over many wave periods or do not correspond to ULF wave energy transport (e.g., contributions to instantaneous **S** due to static current systems can be removed from $\mathbf{S}(f)$ provided the DC and ULF signal are separable).

We tested our calculation of $\mathbf{S}(f)$ using synthetic data to ensure that rounding errors or non-stationary signals do not significantly affect $\mathbf{S}(f)$. In particular, we specified both steady signals and signals with

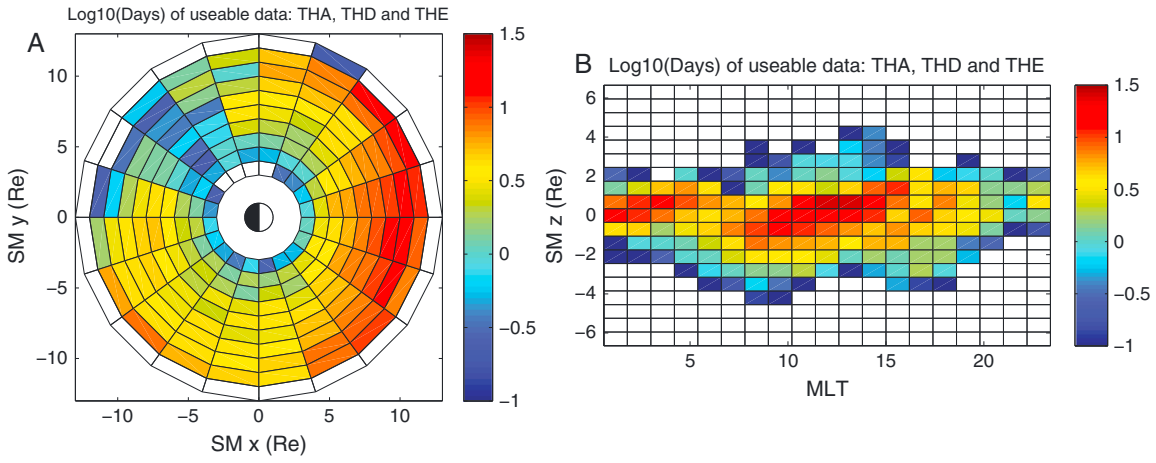

Figure 2. The data coverage from THA, THD, and THE in Log10(days). One day of data is equivalent to 56.25 samples/FFT windows. (a) Data coverage in the SM *xy* plane. (b) Data coverage versus SM *z* position and MLT.

randomly varied phases, durations, periods, and propagation directions, then we calculated the time-averaged Poynting vector in the time domain and compared it to $\mathbf{S}(f)$. After many trials, we found that the two agree very closely even for non-stationary signals, usually within 1% (much lower if the signal is stationary). This suggests that $\mathbf{S}(f)$ can be used without concern that FFT rounding errors or non-stationary ULF signals significantly affect the calculation. The full results of this analysis are in the supporting information.

As in *Hartinger et al.* [2013], we do not use data from all FFT windows; we remove data when (1) the probe is not in the magnetosphere or is too close to the Earth, (2) the length of a data interval is not sufficient to perform the required signal processing (> 60 min), (3) there are numerous spikes or other problems with the 3 s spin fit electric and magnetic field data, (4) the $\mathbf{E} \cdot \mathbf{B} = 0$ assumption is subject to large errors, and (5) electric field measurements are likely to be corrupted (which often occurs when the sun angle, or angle between the spacecraft spin plane and the ecliptic plane, is small, $-1.75° <$ sun angle $< 1.75°$). *Hartinger et al.* [2013] validated the reduced data and demonstrated that no significant systematic errors were present.

Table 2 summarizes the results of each data reduction step for individual THEMIS probes. A large amount of data is removed from the analysis due to large errors in the $\mathbf{E} \cdot \mathbf{B} = 0$ assumption in low-$\mathbf{B}$ regions; these data occur mostly at large L shell (> 10 R_E) in the nightside magnetosphere. These errors are due to division by small values of the spin axis component of the magnetic field, $\mathbf{B}$, leading to large uncertainties in the estimate for the spin axis component of the electric field.

Unique intervals (probes separated by at least 0.5 R_E or the observations are at least 25 min apart) from all probes are combined together. Figure 2 shows data coverage in log10(days) from all probes after all reduction steps have been performed. Figure 2a shows data coverage in the SM *xy* plane; there tends to be more data in the dayside magnetosphere. Data coverage is not uniform in magnetic local time (MLT) for a number of reasons, primarily due to the changes in fast survey mode coverage during the different phases of the THEMIS mission. Figure 2b shows the data coverage versus MLT and SM *z*. The THEMIS satellites' low-inclination orbits cause most measurements to be made within 2 R_E of the dipole equator, with more observations at large geomagnetic latitude in the dayside magnetosphere.

As shown in Figure 2, there are several days of data—or hundreds of samples (1 day is 56.25 samples)—in nearly all spatial regions our study covers. Each sample is unique, or independent, as discussed in the previous paragraph and in *Hartinger et al.* [2013]. Previous studies of ULF waves have used comparable numbers of samples in a given spatial region and obtained realistic results that compare well with theory [e.g., *Takahashi and Anderson*, 1992, Figure 3], so we can proceed with the assumption that we have sufficient measurements to build a representative sample of the ULF wave Poynting vector in each spatial region. It is important to note that most of our measurements were made during solar minimum, so they are more representative of quiet conditions. For this reason, we bin our data using the *Kp* index and focus mostly on results for $Kp \leq 2$.

3.2. Case Study

Figure 3 shows an example data interval used for this study from the THE satellite on 4 March 2013. Figure 3a is for the high pass filtered magnetic field components in FA coordinates, and Figure 3b is for the electric field. All three components of the magnetic field and the two transverse components of the electric field exhibit ~5 mHz (~3 min period) wave activity, indicating a mixture of wave modes at 5 mHz. Figures 3c and 3d are for the power spectral densities of the magnetic field *y* and electric field *x* components, respectively; these components indicate toroidal mode standing Alfvén wave activity. There are clear power enhancements at 5 mHz in both components, and higher-frequency harmonics are also visible in the electric field. The bottom three panels are for the three FA components—*x* (Figure 3e), *y* (Figure 3f) and *z* (Figure 3g), respectively—of $\mathbf{S}(f)$. We show the signed square root of $\mathbf{S}(f)$ to better capture the full range of wave electromagnetic energy flux, as it can be both positive and negative and can vary over many orders of magnitude. Use of the signed square root is purely for convenience when plotting the large range of positive and negative $\mathbf{S}(f)$ here, and this technique is not used elsewhere in this study. The energy flux is predominately in the *z* direction (toward the ionosphere) and is strongest at 5 mHz. Energy is being transferred toward the northern ionosphere (positive *z*) and toward the Earth (negative *x*) for much of the interval.

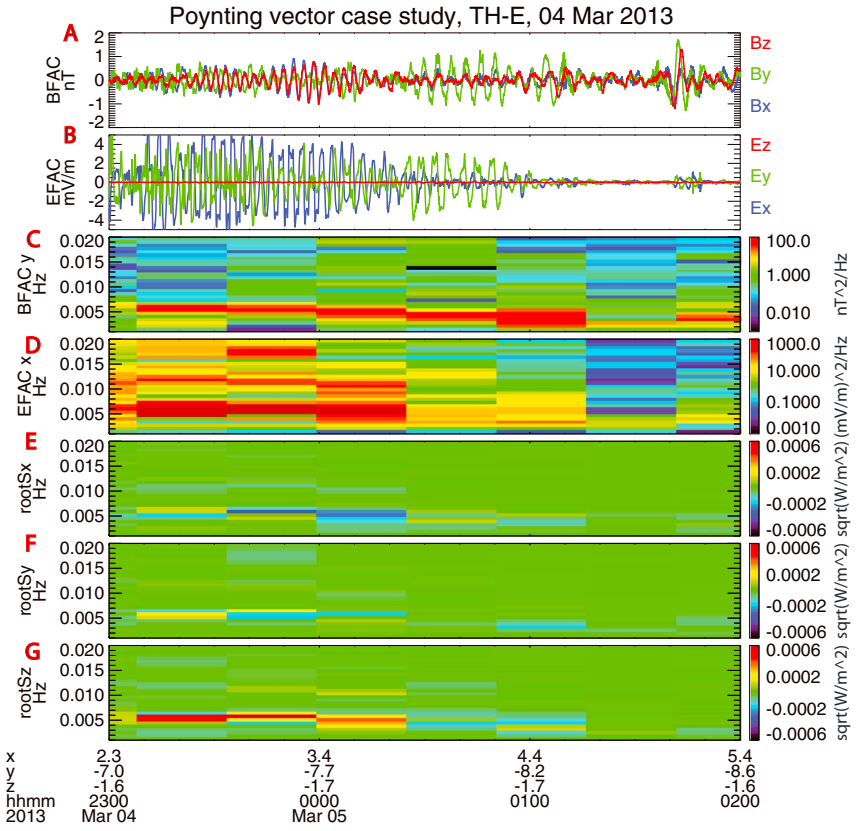

Figure 3. This figure shows an example of Poynting vector observations associated with standing Alfvén waves using the THE probe. The probe GSM position (in Earth radii) and UT label the x axis. (a) Perturbation magnetic field in FA coordinates in which *z* is along the background magnetic field, *y* points eastward, and *x* is approximately radial, (b) Same for electric field, (c) PSD for magnetic field *y* component, (d) Same for electric field *x* component, (e–g) Signed square root of the *x*, *y*, and *z* components of the Poynting vector.

3.3. Low-Signal Events and Statistical Analysis Procedures

Unlike *Hartinger et al.* [2013], we do not remove data when the power spectral densities of the electric or magnetic field are below the noise thresholds of EFI and FGM. The reason is that our results become biased toward higher values for the mean/median $\mathbf{S}(f)$ when we remove these data. This effect is removed by retaining these data and only examining median values or quartiles. The median/quartile results account for these low-signal events and thus are more representative of the true distribution of $\mathbf{S}(f)$ (i.e., the distribution that would be obtained with perfect measurements). At the same time, they reflect geophysical wave activity rather than instrumentation noise provided the noise floor is below the median/quartile.

We examine the 75th percentile (Q_3) of the distribution of $\mathbf{S}(f)$ observations in a given bin (e.g., calculate Q_3 for the distribution of all **S**(6 mHz) observations in the 6–7 MLT sector for $Kp \leq 2$ conditions); the bins vary depending on whether the spatial, frequency, or geomagnetic activity dependence of **S** is being examined. Q_3 is reliable for frequencies below roughly 35 mHz, since less than 75% of the data are removed due to low signal at frequencies below 35 mHz. We use a bootstrap technique [*Efron and Tibshirani*, 1993] to determine a confidence interval for Q_3 and other values used to represent the distribution of **S**(f) observations: (1) we randomly resample the original distribution (with repetition) 1000 times, computing Q_3 for each random sample and (2) we used the distribution of Q_3 from the 1000 resampled data sets to determine a confidence interval (66% or 95%) for the measured value of Q_3. We use these confidence intervals to estimate the uncertainty in our results and determine statistical significance.

Figure 4 shows an example distribution for **S**(6 mHz) measurements for the dayside outer magnetosphere (6 to 18 MLT, dipole *L* from 8 to 13 R_E), $Kp \leq 2$, and equinox conditions (includes days between 4 February and 7 May, and between 5 August and 6 November). It is a histogram of the number of Poynting vector observations as a function of the logarithm of |**S**(6 mHz)|. The distribution is almost log normal; the slight skew to the left is due to our inclusion of events with signals below the noise floor of the instruments.

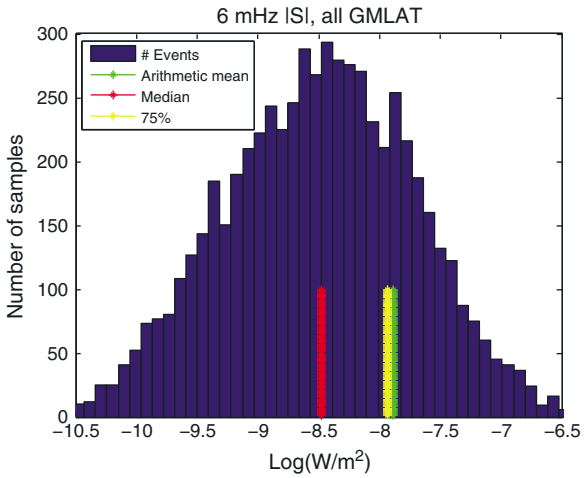

Figure 4. This figure includes 6 mHz Poynting vector measurements between 6 and 18 MLT, 8 and 13 L (R_E), $Kp \leq 2$, and for equinox conditions. The histogram shows the number of events as a function of the logarithm of the Poynting vector magnitude.

The arithmetic mean (green line), median (red line), and Q_3 (yellow line) are also shown on the histogram. The arithmetic mean is skewed to large values (it is well above the median). This further motivates our choice to use quartiles rather than mean values for our statistical analysis of $\mathbf{S}(f)$, as quartiles are much less strongly affected by a few large values of $\mathbf{S}(f)$.

3.4. Procedure/Assumptions for Mapping the Poynting Vector to the Ionosphere

We map the Poynting vector to the ionosphere by tracing along magnetic field lines using different magnetic field models—in this section we discuss how we perform this mapping and what assumptions, caveats, and sources of error are associated with the mapping procedure. We used output from the technique of *Qin et al.* [2007] to obtain parameters necessary for the external magnetic field models. We trace a model magnetic field line from the satellite location to the ionosphere (100 km altitude) and determine the satellite foot point in geographic coordinates, and we use the magnetic field model to calculate the magnetic field magnitude at the foot point ($|B_i|$ in equation (1)) and satellite position ($|B_o|$); we discard any data from locations where the field line tracing or field magnitudes from the model are not physical (e.g., the field line maps to the solar wind). Next, using the measurement of $S_{\|o}$ at the satellite location, we calculate $S_{\|i}$ at the ionosphere using equation (1). Finally, we convert the position of the foot point from geographic coordinates to altitude-adjusted corrected geomagnetic (AACGM) coordinates.

We checked the sensitivity of our results to the choice of field model, using the following combinations of models: (1) International Geomagnetic Reference Field (IGRF) with no external model, (2) IGRF with *Tsyganenko* [1989] model (T89), (3) IGRF with *Tsyganenko and Stern* [1996] model, and (4) IGRF with *Tsyganenko* [2002] model. Results between the first case and last three cases differed noticeably; however, the last three cases were similar both qualitatively and quantitatively. Comparing the magnetic field model output with the THEMIS magnetometer measurement, we found that T89 was overall most consistent with the in situ measurement of field magnitude and direction. Based on these results, we use the T89 model that includes IGRF as the primary tool for mapping in this study.

Regardless of model choice, there will be some error in mapping from HEO to the ionosphere. As noted in previous studies mapping Alfvén waves and also found in this study, this is typically on the order of 1 or 2° in latitude, although this varies depending on region of magnetosphere [e.g., *Keiling et al.*, 2002]. The spatial bins used in this study are larger than or on the order of the expected mapping error length scales, and we shall restrict our interpretation/conclusions to very large scale spatial variations (e.g., the entire dayside magnetosphere, high latitudes versus low latitudes) to reduce the effect of these errors on our analysis. For these reasons, mapping errors do not likely affect the conclusions of this study.

There are three important assumptions required for this mapping to be reliable. One assumption is that energy is going into the ionosphere rather than coming out, in a time average sense. In other words, although wave energy may be reflected from the ionosphere during different portions of a wave cycle, we assume the time average of $S_{\|i}$ at a given frequency over the 25.6 min FFT window, $S_{\|}(f)$, measures only the net ionospheric energy deposition during a wave event. To the best of our knowledge, there is no physical mechanism that could generate ULF $S_{\|}(f)$ directed away from the ionosphere; the ionospheric flywheel—an explanation used by, e.g., *Gary et al.* [1995] to explain $S_{\|i}$ directed away from the ionosphere in LEO—only applies to DC $S_{\|i}$, not AC/ULF (DC refers to frequencies below 3 mHz—see section 1.2), as it invokes horizontal thermospheric neutral winds that do not vary on ULF timescales. *Nishimura et al.* [2010] proposed a mechanism where energy enters the ionosphere at one latitude and exits at other latitudes during sudden commencements; we do not expect this mechanism to substantially affect the results of this study since

we are focusing on frequencies above 3 mHz, whereas the mechanism of *Nishimura et al.* [2010] is for lower-frequency perturbations associated with convection.

Although these physical mechanisms should not generate $S_{\parallel}(f)$ directed away from the ionosphere, transient ULF wave phenomena may generate spurious outgoing $S_{\parallel}(f)$ in events where the 25.6 min FFT window is shorter than or comparable to the transient timescale. The 25.6 min period is significantly longer than the typical transient timescale that precedes standing Alfvén wave/cavity mode/waveguide mode events driven by an impulsive driver. This timescale is on the order of the impulse timescale: typically a few ULF wave periods [*Allan et al.*, 1986]. The longest wave period we consider is 6 min, so our analysis using the 25.6 min FFT window ought to be unaffected by transient events. We further demonstrate this in section 3.1 and the supporting information by calculating $S_{\parallel}(f)$ for synthetic, nonstationary signals.

The second assumption for mapping to be reliable is that all of the electromagnetic energy flux that we initially measure reach the ionosphere. However, some of this electromagnetic energy may be converted to particle kinetic energy before reaching the ionosphere. This energy conversion does not affect our statistical results, as we discuss in section 3.5.

The third assumption for mapping to be reliable is that $S_{\parallel}(f)$ corresponds to a wave mode that is guided by the magnetic field. This assumption is valid for three reasons:

1. Quantitatively, $S_{\parallel o}$ increases with distance from the magnetic equator, as expected from equation (1) if most $S_{\parallel}$ is carried by wave modes that are strongly guided by the magnetic field. We examined Q_3 for $S_{\parallel o}$(6 mHz) versus distance from the T89/IGRF equator, and looked for the expected trend that $S_{\parallel o}$ should scale with the local flux tube cross-sectional area. By dividing a field line into two large bins (0 to 5° and 5 to 15°), there were enough events to observe statistically significant increases in $S_{\parallel o}$(6 mHz) from the lowest geomagnetic latitude bin to the highest geomagnetic latitude bin. For example, for the data in Figure 4, the 95% confidence interval for Q_3 for northward directed $S_{\parallel o}$(6 mHz) in the 0 to 5° bin was 3.7 to 5.2 nW/m^2, whereas the 5 to 15° bin had a 95% confidence interval of 8.0 to 13.0 nW/m^2; thus, there is a statistically significant increase in $S_{\parallel o}$(6 mHz). This trend was present at other frequencies and regardless of whether we considered northward directed Poynting vectors in the region above the magnetic equator or southward directed Poynting vectors in the region below the magnetic equator. This trend is consistent with expectations from equation (1) if most $S_{\parallel}$ is transferred by wave modes that are strongly guided by the magnetic field.
2. Alfvén waves—waves that are theoretically expected to be guided by the magnetic field and thus are well described by equation (1)—are the dominant contributor to $S_{\parallel o}$, suggesting that wave modes that are weakly guided by the magnetic field are at most a minor source of error when statistically analyzing Poynting vector observations using equation (1). Fast mode waves, assuming they have the same amount of energy as Alfvén waves, tend to radiate energy in all directions and thus have reduced $S_{\parallel o}$ when compared to Alfvén waves, which concentrate their energy transfer only along the background field. For fast mode waves to significantly contribute to $S_{\parallel o}$ and be a major source of error in equation (1), they would have to be driven by a nonisotropically radiating source that is strongly asymmetric with respect to the magnetic equator; however, most sources of fast mode wave energy are expected to be symmetric with respect to the magnetic equator [e.g., solar wind pressure pulses, *Takahashi et al.*, 2012].
3. The ionospheric waveguide—which can spread wave energy incident on the ionosphere over a wide range of latitudes and break the assumption that wave energy is guided by the magnetic field—only affects waves with frequencies between roughly 0.1 and 1 Hz. It does not affect the lower frequency waves (3–30 mHz) considered in this study [*Lysak*, 1988b].

In summary, we find that equation (1) is a reliable way of estimating typical energy deposition rates in the ionosphere due to ULF waves. Any sources of error due to deviations from equation (1) are very small relative to the expected variation in the Poynting vector magnitude in different spatial regions and at different frequencies (4 orders of magnitude; Figure 4).

3.5. Assumptions for Estimating Ionospheric Joule Heating Rates

We use the ideal MHD approximation of *Newton et al.* [1978] to estimate ionospheric Joule heating rates by assuming that Joule heating rates exactly match $S_{\parallel i}$. This assumption does not include the physics of the conversion of wave electromagnetic energy flux to particle kinetic energy flux and the generation of kinetic Alfvén waves, which are important for understanding the relationship between ULF waves and the

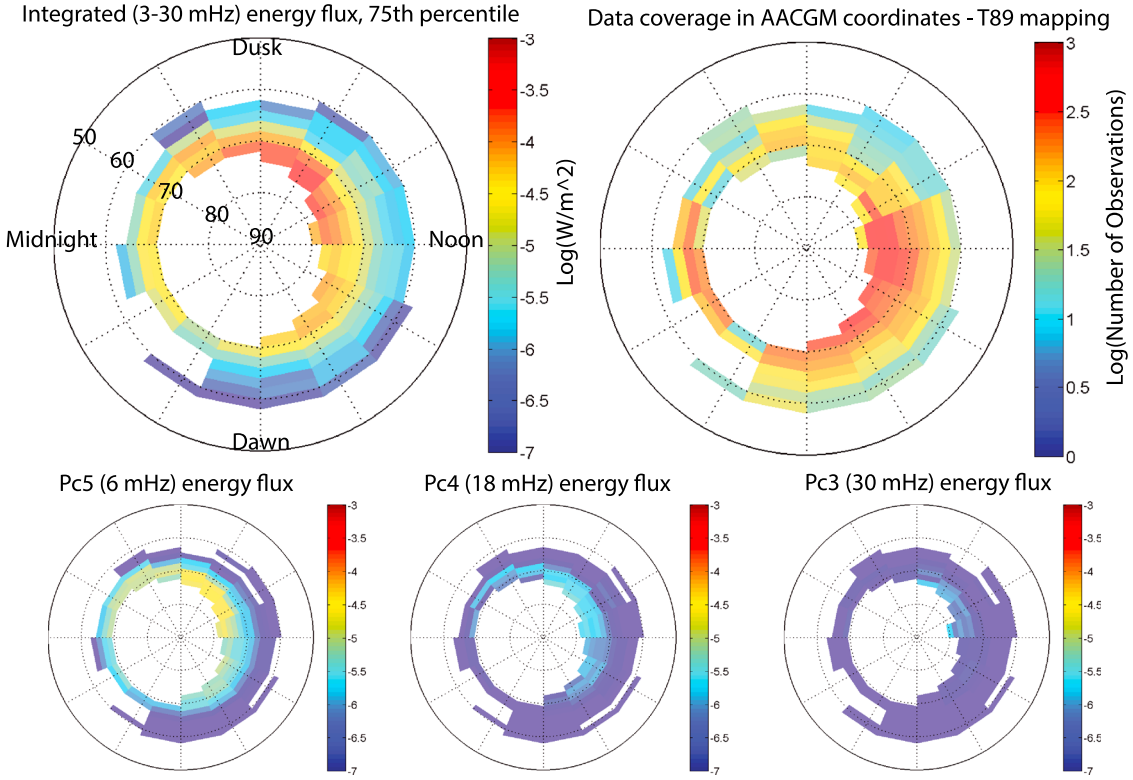

Figure 5. This figure shows spatial distributions of ULF wave energy deposition in the ionosphere. Data from both hemispheres are included for equinox conditions and low geomagnetic activity ($Kp \leq 2$). (top left) Poynting vector data summed over all frequencies in the 3–30 mHz range; the logarithm of Q_3 for the mapped vector data is shown versus AACGM MLT and latitude. (top right) Data coverage (log(number of spectra)). (bottom) Same as Figure 5 (top left), except for Poynting vector data at three discrete frequencies (rather than a sum over frequencies): (from left to right) 6 mHz, 18 mHz, and 30 mHz.

aurora. However, given the complexity of auroral acceleration physics and the expected variability of the acceleration efficiency for different plasma conditions and wave properties [e.g., *Lysak*, 1988a], we postpone analysis of this energy conversion to future studies focused on specific acceleration regimes.

For the purpose of the present study, we regard particle energy conversion as a source of error and we assume that our estimate of the Joule heating rate using *Newton et al.* [1978] is an upper bound, since some wave electromagnetic energy flux ought to be converted to particle energy rather than Joule heating. Based on previous simulation work by *Damiano et al.* [2007], we expect this error to be roughly a factor of 2 or less. *Damiano et al.* [2007] found that 30% of a standing Alfvén wave's initial energy is converted to particle kinetic energy and the rest to Joule heating for a perpendicular wavelength of 0.5 R_E in the equatorial plane, but more energy is converted to particle kinetic energy for smaller perpendicular wavelengths. It is not unreasonable to assume a wavelength of 0.5 R_E or larger, particularly during the initial evolution of a standing Alfvén wave when it is still being driven [*Mann*, 1995, 1997], so a factor of 2 error associated with the ideal MHD assumption of *Newton et al.* [1978] is reasonable. This assumption is further justified by previous studies that found Joule heating was the dominant energy sink for ULF waves in the 3–30 mHz range considered in this study [*Glassmeier et al.*, 1984; *Crowley et al.*, 1985; *Rae et al.*, 2007; *Hartinger et al.*, 2011].

To summarize, we shall regard our estimate of ULF wave Joule heating rates as an upper bound, and we shall not emphasize spatial, frequency, or geomagnetic activity variations in the Joule heating rate that are smaller than a factor of 2.

4. Results

Having determined that equation (1) can be used to statistically map the Poynting vector to the ionosphere, we now use this equation to quantify the spatial, frequency, and geomagnetic activity level dependence of ULF wave energy deposition in the ionosphere. In this section, we map $S_{\|o}$ to the ionosphere using magnetic field models for both B_i and B_o and to determine the location of the satellite foot point. If $S_{\|o}$ is positive,

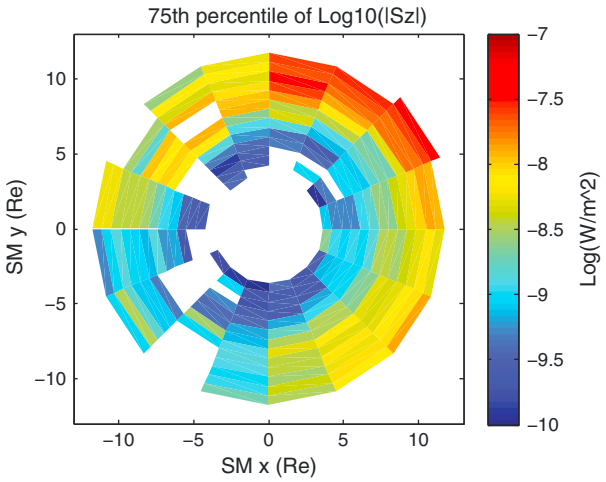

Figure 6. This figure is for the same conditions as in Figure 5 (equinox, $Kp \leq 2$). The logarithm of Q_3 for $|S_{\|o}(6\text{ mHz})|$ is shown versus SM *xy* position.

we map it to the Northern Hemisphere; if negative, the Southern Hemisphere. The sign of $S_{\|o}$ is a reliable indicator of the direction of net energy transfer since the 25.6 min FFT window used to compute $S_{\|o}$ is roughly 5 times longer than the longest wave period examined (see section 3.4/3.1 and supporting information for further discussion).

Obtaining $S_{\|i}$ using equation (1), we found that energy deposition results in the Northern Hemisphere were very similar to the Southern Hemisphere during equinox conditions. In the remainder of this section, we will combine data from both hemispheres and focus on equinox conditions. We also examined winter and summer conditions, finding differences between the northern and southern ionospheric energy deposition rates; however, these results are beyond the scope of the present work and will be discussed more fully in a future study.

4.1. Spatial Dependence of ULF Wave Ionospheric Energy Deposition

Figure 5 shows the spatial variation of ULF wave energy deposition rates in the ionosphere at a variety of frequencies using the T89 model for mapping. Data from both hemispheres are included for equinox conditions and low geomagnetic activity ($Kp \leq 2$). Figure 5 (top right) is for the data coverage in terms of the logarithm of the number of spectra (observations). The lack of data coverage at high latitudes on the nightside is mostly due to restrictions on using the $\mathbf{E} \cdot \mathbf{B} = 0$ approximation (see section 3).

Figure 5 (top left) is for $S_{\|i}$ summed over all frequencies in the 3–30 mHz frequency range; it is thus a measure of the total ULF or AC (3–30 frequency mHz band) contribution to energy deposition rates. The logarithm of Q_3 for the distribution $S_{\|i}$ in a given AACGM MLT/latitude bin is shown in Figure 5 (top left). ULF energy deposition rates on the order of 0.1–1 mW/m^2 are common at high latitudes, with lower rates at lower latitudes. As shown in the distribution of $S_{\|o}$ in Figure 4, energy transfer rates are highly variable—ranging over roughly 4 orders of magnitude. Median values of $S_{\|i}$ are roughly a factor of 5 lower than the results for Q_3, as shown in Figure 5, whereas maximum values may be 2 orders of magnitude larger.

Figure 5 (bottom panels) are the same format as the top left, except they are for Poynting vector data at three discrete frequencies (rather than a sum over frequencies): 6 mHz, 18 mHz, and 30 mHz (from left to right). At all frequencies, most energy deposition occurs in the dayside/postnoon sector and at higher latitudes (note that the longitudinal dependence of energy deposition rates is not due to magnetic latitude sampling bias, as shown in the supporting information). More energy is deposited at lower frequencies when compared to higher frequencies. The spatial variation of energy deposition rates is consistent with what is observed in the magnetosphere. For example, Figure 6 shows Q_3 for $|S_{\|o}$ (6 mHz)| versus SM *xy* position. Near the equatorial plane, larger parallel Poynting vectors are seen at 6 mHz at larger radial distances and in the noon/postnoon sector, qualitatively consistent with the results that would be obtained if a dipole model were used to map $S_{\|o}$ to the ionosphere. This comparison suggests that our use of an empirical model (T89) to map $S_{\|o}$ to the ionosphere does not substantially affect $S_{\|i}$.

The peak in the postnoon sector and at high latitudes is likely due to (1) the presence of standing Alfvén waves driven by magnetopause surface waves (amplitudes decay with distance from magnetopause/at lower latitudes) and (2) a dawn-dusk asymmetry in electron precipitation that leads to an asymmetry in the Pedersen conductivity (minimum postnoon) near the auroral oval [*Hardy et al.*, 1987]. The $S_{\|i}$ peak postnoon and at high latitudes is expected if a solar wind pressure pulse excites surface wave perturbations that are symmetric with respect to noon and carry equal amounts of energy toward the dawn and dusk sectors. In this case, more energy will be deposited at higher latitudes where the surface wave amplitude (and resultant standing Alfvén wave amplitude) is largest. Also, more energy will be lost in the low-conductivity dusk

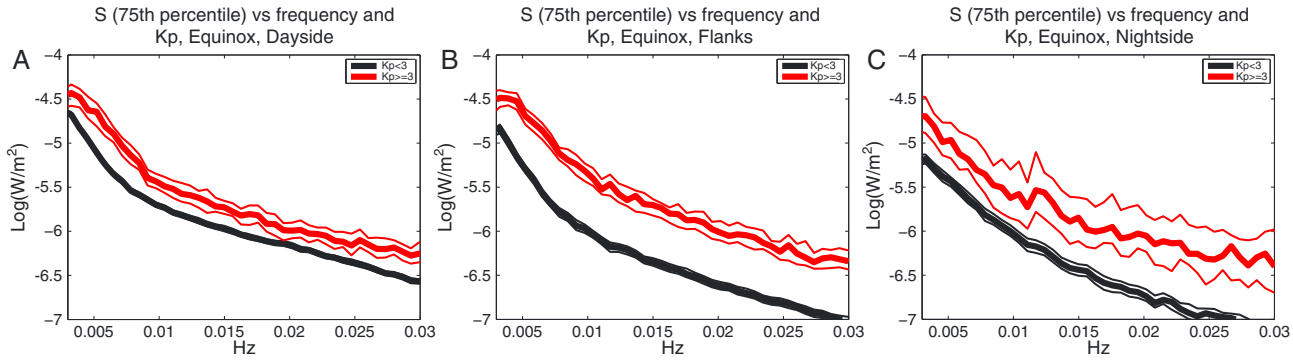

Figure 7. This figure shows the *Kp* and frequency dependence of ULF wave energy deposition in different local time sectors. (a) Q_3 for the mapped Poynting vector as a function of frequency for the dayside sector ($8 < \text{MLT} \leq 16$) for two *Kp* ranges: $Kp < 3$ (black line) and $Kp \geq 3$ (red line). Error bars (faint lines) indicate the 95% confidence interval for Q_3. (b) The same as Figure 7a but for the flank region ($4 \leq \text{MLT} < 8$ or $16 \leq \text{MLT} < 20$). (c) The same as Figures 7a and 7b but for the nightside MLT sector ($\text{MLT} > 20$ or $\text{MLT} \leq 4$).

sector before the surface wave reaches the dawn-dusk terminator since the standing Alfvén wave damping rate is larger in low-conductivity regions [*Newton et al.*, 1978], leading to the postnoon peak in $S_{\|i}$.

Takahashi and Anderson [1992] found a statistically significant postnoon peak in power spectral density (PSD) in magnetic field components consistent with standing Alfvén waves; this was different than previous studies finding a prenoon/dawn peak in standing Alfvén wave occurrence rates (rather than PSD), and *Takahashi and Anderson* [1992] attributed this difference to contributions to PSD made by events that were not classified as monochromatic standing Alfvén waves. This explanation also reconciles the results of the present study with previous studies finding peak occurrence rates of standing Alfvén waves outside the postnoon sector. The low ionospheric conductivities in the postnoon sector [*Hardy et al.*, 1987] make it a poor resonator for standing Alfvén waves when compared to higher conductivity regions, such as the prenoon sector; one thus expects postnoon standing Alfvén waves to be more strongly damped and have a broader-frequency spectrum when compared to dawn sector waves [*Newton et al.*, 1978]. They will also be less prominent in studies focused on narrow spectral features compared to studies lacking this focus and examining the parallel Poynting vector or averaged PSD.

4.2. Geomagnetic Activity and Frequency Dependence of Energy Deposition

Figure 7 shows the *Kp* and frequency dependence of ULF wave energy deposition in different local time sectors. Like Figure 5, this is for equinox conditions and the T89 model is used to map the Poynting vector to the ionosphere. Data from all latitudes are binned together. Figure 7a shows Q_3 for the mapped Poynting vector as a function of frequency in the dayside sector ($8 < \text{MLT} \leq 16$) for two *Kp* ranges: $Kp < 3$ (black line) and $Kp \geq 3$ (red line). Error bars (faint lines) are obtained using the bootstrap technique (see section 3.3). For both low and high geomagnetic activity levels, the energy deposition rate decreases with increasing frequency. Finally, Figure 7a shows that there is a statistically significant difference between low and high geomagnetic activity rates at all frequencies.

Figure 7b is the same as Figure 7a but for the flank region ($4 \leq \text{MLT} < 8$ or $16 \leq \text{MLT} < 20$). In this local time sector, energy deposition also decreases with increasing frequency. The *Kp* dependence is stronger than on the dayside, with Q_3 roughly a factor of 3–5 larger during active conditions. Energy deposition in the flanks is lower than the dayside magnetosphere during quiet conditions but comparable during active conditions.

Finally, Figure 7c is the same as Figures 7a and 7b but for the nightside MLT sector ($\text{MLT} > 20$ or $\text{MLT} \leq 4$). *Kp* dependence is similar to the dayside magnetosphere. Energy deposition rates decrease with increasing frequency, as in the other MLT sectors. They are also generally lower in this sector when compared to the other two local time sectors; this may be partly due to the lack of data from high latitudes in the nightside region. However, these lower rates are also due to the MLT dependence of typical drivers of ULF wave activity: large amplitude ULF waves tend to be observed in the dayside and flank regions, particularly at low frequencies. Additionally, lower rates for $S_{\|i}$ are expected near midnight, where the ULF wave Poynting vector tends to be oriented perpendicular to the magnetic field and less energy is directed toward the ionosphere [*Hartinger et al.*, 2013].

To summarize Figure 7, energy deposition rates decrease with increasing frequency in all local time sectors. The strongest *Kp* dependence is in the flank region, with weaker dependency in the dayside and nightside magnetosphere. In all cases, energy deposition rates increase during more active conditions. They are typically a factor of 3–5 larger during active conditions in the flank region, whereas in other sectors this difference is smaller.

5. Discussion

In this section, we relate our observations in section 4 to Joule heating impacts in the ionosphere. We use the ideal MHD approximation of *Newton et al.* [1978] to estimate ionospheric Joule heating rates by assuming these rates exactly match $S_{\|i}$, as discussed in section 3.5. Table 1 shows that typical values for $S_{\|i}$/Joule heating in this study, when considering all latitudes ($60 > \Lambda > 80$) and low geomagnetic activity conditions ($Kp \leq 2$), are 0.001–1 mW/m^2, comparable to other studies of Joule heating associated with standing Alfvén waves [*Rae et al.*, 2007; *Hartinger et al.*, 2011]. However, these values are smaller than what is typically observed by LEO satellites for $S_{\|i}$/Joule heating. Since LEO satellite observations are usually a mixture of DC and AC $S_{\|i}$ (see section 1.2 for further explanation and definitions for DC and AC), one interpretation of the larger Joule heating rates found at LEO is that the DC Joule heating rate is much larger than the AC Joule heating rate. To test whether this interpretation is correct, we require estimates of the DC Joule heating rate, rather than a mixture of AC and DC rates.

The *Weimer* [2005] empirical model provides such estimates. It is based on electric and magnetic field observations from a LEO satellite, but it also requires the assumption that the global electric potential pattern remains static on timescales of 15–20 min. Variations with smaller timescales are smoothed out during the process of obtaining the electric potential [e.g., *Shue and Weimer*, 1994, Figure 1]. Thus, this model is sensitive only to the DC Joule heating rate, and it provides a benchmark for comparing the AC (ULF) and DC Joule heating rates.

The DC Joule heating in the *Weimer* [2005] model comes primarily from the dissipation of large-scale current systems generated by plasma transport in the magnetosphere. These are the same current systems described by *Iijima and Potemra* [1978], as can be seen by comparing the spatial pattern for the field-aligned current intensity for southward IMF conditions found by *Weimer* [2005] (Figure 4 in that study) to the pattern found by *Iijima and Potemra* [1978] (Figure 13 in that study). The global structure of these currents changes on timescales longer than the integration time required for the *Weimer* [2005] model (15–20 min), and they can be considered static when compared to ULF wave timescales (minutes).

Comparing Figure 5 in *Weimer* [2005] with Figure 5 in this study, it is clear that AC (ULF) Joule heating rates are typically smaller than DC Joule heating rates. This is particularly true during southward IMF conditions, when there are regions with nominal DC heating rates as large as 19 mW/m^2. The contributions of these intense heating regions to the global, integrated Joule heating rate are more important than nominal ULF wave contributions of 0.001–1 mW/m^2. This is also true to a lesser extent for other geomagnetic conditions, with the possible exception of periods with northward IMF when DC heating rates are smallest [*Weimer*, 2005, Figure 5]. This is a major finding of this study: nominally, ULF waves do not make significant contributions to the global Joule heating rate when compared to large-scale, static current systems. This result partially confirms the prediction of *Dessler* [1959b] that ULF waves are nominally not an important heat source for the ionosphere, with the caveat that the importance of the ULF wave contribution depends on how accurately one needs to determine ionosphere/thermosphere temperatures. As noted by *Greenwald and Walker* [1980], the values predicted by *Dessler* [1959b] for ULF wave heating rates are very low due to an assumption of a high ULF wave frequency (1 Hz). Lower frequency (3–30 mHz) ULF wave heating rates of 0.001–1 mW/m^2 affect ionosphere/thermosphere temperatures—particularly if wave activity is spread over a larger region [e.g., *Rae et al.*, 2007]—but their effect is usually small compared to large-scale, static currents.

A second finding of this study is that ULF waves can make important contributions to the global Joule heating rate during extreme events. Figure 4 shows that there are ULF wave events with $S_{\|}$ more than an order of magnitude larger than the upper quartile; the integrated (over 3–30 mHz band) AC $S_{\|i}$ in these events is on the order of 10 mW/m^2, comparable to the large, localized DC Joule heating rates found by *Weimer* [2005]. These events are more likely to occur during geomagnetically active (high *Kp*) periods, as indicated in Figure 7 by the statistical preference for larger $S_{\|i}$ at all frequencies. Returning to the results of

Table 1, it is clear that other studies also found cases with extremely large ≥100 mW/m^2 $S_{\|i}$ associated with ULF waves, though at least a few of these cases were not standing Alfvén waves and/or they occurred in different regions of the magnetosphere than those considered in the present study [*Angelopoulos et al.*, 2002; *Wygant et al.*, 2002; *Keiling et al.*, 2002, 2003].

A third finding of this study is that ULF waves—in particular, low-frequency waves—make important contributions to regional Joule heating rates even during nominal conditions. The DC Joule heating patterns shown in Figure 5 of *Weimer* [2005] for different IMF clock angles differ substantially from the pattern for the integrated AC Joule heating rate shown in Figure 5 of this study. In other words, the spatial dependence for energy deposition due to ULF waves (frequency > 3 mHz), which mostly comes from standing Alfvén waves (section 1.1), does not match the spatial dependence due to large-scale, static (frequency < 3 mHz) current systems driven by convection in the magnetosphere. In local time sectors/latitudes where contributions to Joule heating from large-scale static current systems are small, ULF waves contribute more to the overall Joule heating rate. Based on the comparison between Figure 5 in *Weimer* [2005] and Figure 5 in this study, ULF waves make their largest relative contribution to the Joule heating rate near noon and midnight, where DC heating rates are often close to 0, whereas AC heating is close to 1 mW/m^2; in other words, the ratio of the AC to DC Joule heating rates is largest in these regions. Finally, Figures 5 and 7 in this study demonstrate that ULF wave energy deposition in the ionosphere is largest at low frequencies in all local time sectors. This suggests that low-frequency Pc5 waves (<7 mHz) are the most important contributor to the AC Joule heating rate, and periods with enhanced Pc5 wave activity ought to have the largest AC/DC Joule heating ratios.

Finally, we note that in a similar study, *Janhunen et al.* [2005] found that the "AC" $S_{\|i}$ was significantly smaller than the "DC" rate, but their study was focused on the auroral acceleration implications of $S_{\|i}$ (rather than Joule heating) and had several key differences from this one: (1) only periods when the satellite was conjugate to the nominal auroral oval were included (18–6 MLT, 65–74 invariant latitude), (2) there was no restriction to closed field line regions, (3) use of a satellite with a high-inclination orbit (Polar), (4) the "AC" definition differs from this study and refers to three different categories of measurements corresponding to different time domain filter cutoffs (two of which roughly correspond to the ULF wave frequencies examined in the present study). For these reasons, some of their results differ substantially from this study; in particular, the spatial patterns found for AC Joule heating in Figure 6 of *Janhunen et al.* [2005] are different than in Figure 5 in this study. Nevertheless, their overall conclusion that AC $S_{\|i}$ is smaller than DC $S_{\|i}$ is consistent with the results of this study for nominal conditions, and the typical values they found for $S_{\|i}$ are in agreement with those found in this study (Table 1).

6. Summary

We presented results of the spatial, frequency, and geomagnetic activity dependence of ULF wave (3–30 mHz) electromagnetic energy flux into the ionosphere. In particular, we statistically analyzed the energy flux using Q3 (upper quartile) rather than mean/median values since Q3 is above the noise at all frequencies under consideration and is not biased by large events. We used the T89 magnetic field model to map the Poynting vector to the ionosphere, validating this mapping using comparisons with other models, THEMIS satellite data, and several tests showing equation (1) can be used to estimate typical ULF wave energy deposition rates in the ionosphere. Using the ideal MHD model of *Newton et al.* [1978] to directly relate these energy deposition rates to AC Joule heating rates in the ionosphere, we obtained several key results:

1. AC Joule heating due to ULF waves tends to be largest at low frequencies and high latitudes.
2. Typical heating rates are on the order of 0.001–1 mW/m^2 and can vary by a few orders of magnitude in a given spatial region. Compared to the *Weimer* [2005] empirical model of DC Joule heating rates, these values suggest that ULF waves nominally make small contributions to the global, integrated Joule heating rate when compared to contributions from large-scale, static (DC) current systems. These results are mostly in agreement with the predictions of *Dessler* [1959b] for higher-frequency (1 Hz) ULF waves.
3. The ULF wave contribution to the global Joule heating rate is substantial during extreme events, which tend to occur during active conditions ($Kp \geq 3$). For example, nominal ULF wave energy deposition rates (Q3) increase from 0.01 to 0.03 mW/m^2 at Pc5 frequencies (near 5 mHz) and from 0.001 to 0.005 mW/m^2

at Pc4 frequencies (near 10 mHz) during dawn sector active periods. The noon and midnight local time sectors have weaker activity dependence compared to the flank regions.

4. A postnoon peak in ULF wave energy deposition rates is likely associated with reduced ionospheric conductivities in this region [*Hardy et al.*, 1987].
5. With regard to local Joule heating, the ratio of the AC (ULF) and DC Joule heating rates is largest near noon and midnight. In these regions, ULF waves nominally make significant contributions to overall Joule heating rates. The largest contributions to the AC/ULF Joule heating rate comes from lower frequency Pc5 ULF waves; thus, we expect periods with enhanced Pc5 wave activity to have the largest AC/DC Joule heating ratios.

Acknowledgments

M. D. Hartinger was supported by NSF grant AGS-1230398. M.B. Moldwin was partially supported by NASA LWS NNX10AQ53G. S. Zou was partially supported by NSF AGS-1203232. We acknowledge NASA THEMIS contract NAS5-02099 and thank C. W. Carlson and J. P. McFadden for the use of the ESA data, D. Larson and R.P. Lin for the use of SST data, J. W. Bonnell and F. S. Mozer for use of EFI data, and K. H. Glassmeier, U. Auster, and W. Baumjohann for the use of FGM data provided under the lead of the Technical University of Braunschweig and with financial support through the German Ministry for Economy and Technology and the German Center for Aviation and Space (DLR) under contract 50 OC 0302. We thank the NASA Space Science Data facility for use of solar wind data and geomagnetic activity indices. We thank Haje Korth for providing the Geopack interface as part of the TDAS software package, and Kolya Tsyganenko for creating the Geopack library and external field models. Magnetic field input parameters (derived from data on OMNIWeb) were provided by Richard Denton and Zhengui Qin. We thank Margaret Kivelson, Richard Denton, and Jonathan Rae for suggestions on data visualization and interpretation. Data and the TDAS software package used for this study can be obtained from the THEMIS website (http://themis.ssl.berkeley.edu/index.shtml, softwareversion2013-09-12). We thank the reviewers for their time and effort in reviewing this paper.

Michael Balikhin thanks the reviewers for their assistance in evaluating this paper.

References

Allan, W., S. P. White, and E. M. Poulter (1986), Impulse-excited hydromagnetic cavity and field-line resonances in the magnetosphere, *Planet. Space Sci.*, *34*, 371–385, doi:10.1016/0032-0633(86)90144-3.

Anderson, B. J., M. J. Engebretson, and L. J. Zanetti (1989), Distortion effects in spacecraft observations of MHD toroidal standing waves—Theory and observations, *J. Geophys. Res.*, *94*, 13,425–13,445, doi:10.1029/JA094iA10p13425.

Anderson, B. J., M. J. Engebretson, S. P. Rounds, L. J. Zanetti, and T. A. Potemra (1990), A statistical study of Pc 3–5 pulsations observed by the AMPTE/CCE magnetic fields experiment. I. Occurrence distributions, *J. Geophys. Res.*, *95*, 10,495–10,523, doi:10.1029/JA095iA07p10495.

Angelopoulos, V., J. A. Chapman, F. S. Mozer, J. D. Scudder, C. T. Russell, K. Tsuruda, T. Mukai, T. J. Hughes, and K. Yumoto (2002), Plasma sheet electromagnetic power generation and its dissipation along auroral field lines, *J. Geophys. Res.*, *107*(A8), 1181, doi:10.1029/2001JA900136.

Auster, H. U., et al. (2008), The THEMIS fluxgate magnetometer, *Space Sci. Rev.*, *141*, 235–264, doi:10.1007/s11214-008-9365-9.

Bonnell, J. W., F. S. Mozer, G. T. Delory, A. J. Hull, R. E. Ergun, C. M. Cully, V. Angelopoulos, and P. R. Harvey (2008), The Electric Field Instrument (EFI) for THEMIS, *Space Sci. Rev.*, *141*, 303–341, doi:10.1007/s11214-008-9469-2.

Chaston, C. C., et al. (2005), Energy deposition by Alfvén waves into the dayside auroral oval: Cluster and FAST observations, *J. Geophys. Res.*, *110*, A02211, doi:10.1029/2004JA010483.

Codrescu, M. V., T. J. Fuller-Rowell, and J. C. Foster (1995), On the importance of E-field variability for Joule heating in the high-latitude thermosphere, *Geophys. Res. Lett.*, *22*, 2393–2396, doi:10.1029/95GL01909.

Cosgrove, R. B., M. Alhassan, Y. Xu, M. Van Welie, J. Rehberger, S. Musielak, and N. Cahill (2014), Empirical model of Poynting flux derived from FAST data and a cusp signature, *J. Geophys. Res. Space Physics*, *119*, 411–430, doi:10.1002/2013JA019105.

Crowley, G., N. Wade, J. A. Waldock, T. R. Robinson, and T. B. Jones (1985), High time-resolution observations of periodic frictional heating associated with a Pc5 micropulsation, *Nature*, *316*, 528–530, doi:10.1038/316528a0.

Damiano, P. A., A. N. Wright, R. D. Sydora, and J. C. Samson (2007), Energy dissipation via electron energization in standing shear Alfvén waves, *Phys. Plasmas*, *14*, 062904, doi:10.1063/1.2744226.

Dessler, A. J. (1959a), Upper atmosphere density variations due to hydromagnetic heating, *Nature*, *184*, 261–262, doi:10.1038/184261b0.

Dessler, A. J. (1959b), Ionospheric heating by hydromagnetic waves, *J. Geophys. Res.*, *64*(4), 397–401, doi:10.1029/JZ064i004p00397.

Dombeck, J., C. Cattell, J. R. Wygant, A. Keiling, and J. Scudder (2005), Alfvén waves and Poynting flux observed simultaneously by Polar and FAST in the plasma sheet boundary layer, *J. Geophys. Res.*, *110*, A12S90, doi:10.1029/2005JA011269.

Dungey, J. W. (1967), Hydromagnetic waves, in *Physics of Geomagnetic Phenomena*, edited by S. Matsushita and W. H. Campbell, Academic, New York.

Efron, B., and R. J. Tibshirani (1993), *An Introduction to the Bootstrap*, CRC Press, Boca Raton, Fla.

Frey, S., V. Angelopoulos, M. Bester, J. Bonnell, T. Phan, and D. Rummel (2008), Orbit design for the THEMIS mission, *Space Sci. Rev.*, *141*, 61–89, doi:10.1007/s11214-008-9441-1.

Fuller-Rowell, T. J., M. V. Codrescu, R. J. Moffett, and S. Quegan (1994), Response of the thermosphere and ionosphere to geomagnetic storms, *J. Geophys. Res.*, *99*, 3893–3914, doi:10.1029/93JA02015.

Gary, J. B., R. A. Heelis, and J. P. Thayer (1995), Summary of field-aligned Poynting flux observations from DE 2, *Geophys. Res. Lett.*, *22*, 1861–1864, doi:10.1029/95GL00570.

Glassmeier, K. H., H. Volpers, and W. Baumjohann (1984), Ionospheric Joule dissipation as a damping mechanism for high latitude ULF pulsations—Observational evidence, *Planet. Space Sci.*, *32*, 1463–1466, doi:10.1016/0032-0633(84)90088-6.

Greenwald, R. A., and A. D. M. Walker (1980), Energetics of long period resonant hydromagnetic waves, *Geophys. Res. Lett.*, *7*, 745–748, doi:10.1029/GL007i010p00745.

Hardy, D. A., M. S. Gussenhoven, R. Raistrick, and W. J. McNeil (1987), Statistical and functional representations of the pattern of auroral energy flux, number flux, and conductivity, *J. Geophys. Res.*, *92*, 12,275–12,294, doi:10.1029/JA092iA11p12275.

Hartinger, M., V. Angelopoulos, M. B. Moldwin, K.-H. Glassmeier, and Y. Nishimura (2011), Global energy transfer during a magnetospheric field line resonance, *Geophys. Res. Lett.*, *38*, L12101, doi:10.1029/2011GL047846.

Hartinger, M. D., M. B. Moldwin, K. Takahashi, J. W. Bonnell, and V. Angelopoulos (2013), Survey of the ULF wave Poynting vector near the Earth's magnetic equatorial plane, *J. Geophys. Res. Space Physics*, *118*, 6212–6227, doi:10.1002/jgra.50591.

Hughes, W. J., and D. J. Southwood (1976), The screening of micropulsation signals by the atmosphere and ionosphere, *J. Geophys. Res.*, *81*, 3234–3240, doi:10.1029/JA081i019p03234.

Iijima, T., and T. A. Potemra (1978), Large-scale characteristics of field-aligned currents associated with substorms, *J. Geophys. Res.*, *83*, 599–615, doi:10.1029/JA083iA02p00599.

Jacobs, J. A., Y. Kato, S. Matsushita, and V. A. Troitskaya (1964), Classification of geomagnetic micropulsations, *J. Geophys. Res.*, *69*, 180–181, doi:10.1029/JZ069i001p00180.

Janhunen, P., A. Olsson, N. A. Tsyganenko, C. T. Russell, H. Laakso, and L. G. Blomberg (2005), Statistics of a parallel Poynting vector in the auroral zone as a function of altitude using Polar EFI and MFE data and Astrid-2 EMMA data, *Ann. Geophys.*, *23*, 1797–1806, doi:10.5194/angeo-23-1797-2005.

Keiling, A. (2009), Alfvén waves and their roles in the dynamics of the Earth's magnetotail: A review, *Space Sci. Rev.*, *142*, 73–156, doi:10.1007/s11214-008-9463-8.

Keiling, A., J. R. Wygant, C. Cattell, W. Peria, G. Parks, M. Temerin, F. S. Mozer, C. T. Russell, and C. A. Kletzing (2002), Correlation of Alfvén wave Poynting flux in the plasma sheet at 4–7 R_E with ionospheric electron energy flux, *J. Geophys. Res.*, *107*(A7), 1132, doi:10.1029/2001JA900140.

Keiling, A., J. R. Wygant, C. A. Cattell, F. S. Mozer, and C. T. Russell (2003), The global morphology of wave Poynting flux: Powering the aurora, *Science*, *299*, 383–396, doi:10.1126/science.1080073.

Kivelson, M. G., and C. T. Russell (Ed.) (1995), *Introduction to Space Physics*, Cambridge Univ. Press, Cambridge, U. K.

Knipp, D., S. Eriksson, L. Kilcommons, G. Crowley, J. Lei, M. Hairston, and K. Drake (2011), Extreme Poynting flux in the dayside thermosphere: Examples and statistics, *Geophys. Res. Lett.*, *38*, L16102, doi:10.1029/2011GL048302.

Lathuillere, C., F. Glangeaud, and Z. Y. Zhao (1986), Ionospheric ion heating by ULF Pc5 magnetic pulsations, *J. Geophys. Res.*, *91*, 1619–1626, doi:10.1029/JA091iA02p01619.

Le, G., P. J. Chi, R. J. Strangeway, and J. A. Slavin (2011), Observations of a unique type of ULF wave by low-altitude space technology 5 satellites, *J. Geophys. Res.*, *116*, A08203, doi:10.1029/2011JA016574.

Lysak, R. L. (1988a), Electrodynamic coupling of the magnetosphere and ionosphere, *Space Sci. Rev.*, *52*, 33–87, doi:10.1007/BF00704239.

Lysak, R. L. (1988b), Theory of auroral zone PiB pulsation spectra, *J. Geophys. Res.*, *93*, 5942–5946, doi:10.1029/JA093iA06p05942.

Mann, I. R. (1995), Coupling of magnetospheric cavity modes to field line resonances: A study of resonance widths, *J. Geophys. Res.*, *100*, 19,441–19,456, doi:10.1029/95JA00820.

Mann, I. R. (1997), On the internal radial structure of field line resonances, *J. Geophys. Res.*, *102*, 27,109–27,119, doi:10.1029/97JA02385.

McFadden, J. P., C. W. Carlson, D. Larson, M. Ludlam, R. Abiad, B. Elliott, P. Turin, M. Marckwordt, and V. Angelopoulos (2008), The THEMIS ESA plasma instrument and in-flight calibration, *Space Sci. Rev.*, *141*, 277–302, doi:10.1007/s11214-008-9440-2.

Newton, R. S., D. J. Southwood, and W. J. Hughes (1978), Damping of geomagnetic pulsations by the ionosphere, *Planet. Space Sci.*, *26*, 201–209, doi:10.1016/0032-0633(78)90085-5.

Nishimura, Y., T. Kikuchi, A. Shinbori, J. Wygant, Y. Tsuji, T. Hori, T. Ono, S. Fujita, and T. Tanaka (2010), Direct measurements of the Poynting flux associated with convection electric fields in the magnetosphere, *J. Geophys. Res.*, *115*, A12212, doi:10.1029/2010JA015491.

Olsson, A., P. Janhunen, T. Karlsson, N. Ivchenko, and L. Blomberg (2004), Statistics of Joule heating in the auroral zone and polar cap using Astrid-2 satellite Poynting flux, *Ann. Geophys.*, *22*, 4133–4142, doi:10.5194/angeo-22-4133-2004.

Qin, Z., R. E. Denton, N. A. Tsygnanenko, and S. Wolf (2007), Solar wind parameters for magnetospheric magnetic field modeling, *Space Weather*, *5*, S11003, doi:10.1029/2006SW000296.

Rae, I. J., C. E. J. Watt, F. R. Fenrich, I. R. Mann, L. G. Ozeke, and A. Kale (2007), Energy deposition in the ionosphere through a global field line resonance, *Ann. Geophys.*, *25*, 2529–2539, doi:10.5194/angeo-25-2529-2007.

Sibeck, D. G., and V. Angelopoulos (2008), THEMIS science objectives and mission phases, *Space Sci. Rev.*, *141*, 35–59, doi:10.1007/s11214-008-9393-5.

Singer, H. J., D. J. Southwood, R. J. Walker, and M. G. Kivelson (1981), Alfven wave resonances in a realistic magnetospheric magnetic field geometry, *J. Geophys. Res.*, *86*, 4589–4596, doi:10.1029/JA086iA06p04589.

Shue, J. H., and D. R. Weimer (1994), The relationship between ionospheric convection and magnetic activity, *J. Geophys. Res.*, *99*, 401–416, doi:10.1029/93JA01946.

Strangeway, R. J., R. E. Ergun, Y. J. Su, C. W. Carlson, and R. C. Elphic (2005), Factors controlling ionospheric outflows as observed at intermediate altitudes, *J. Geophys. Res.*, *110*, A03221, doi:10.1029/2004JA010829.

Takahashi, K., and B. J. Anderson (1992), Distribution of ULF energy (f < 80 mHz) in the inner magnetosphere—A statistical analysis of AMPTE CCE magnetic field data, *J. Geophys. Res.*, *97*, 10,751–10,773, doi:10.1029/92JA00328.

Takahashi, K., K. Yumoto, S. G. Claudepierre, E. R. Sanchez, O. A Troshichev, and A. S. Janzhura (2012), Dependence of the amplitude of Pc5-band magnetic field variations on the solar wind and solar activity, *J. Geophys. Res.*, *117*, A04207, doi:10.1029/2011JA017120.

Tsyganenko, N. A. (1989), A magnetospheric magnetic field model with a warped tail current sheet, *Planet. Space Sci.*, *37*, 5–20, doi:10.1016/0032-0633(89)90066-4.

Tsyganenko, N. A. (2002), A model of the near magnetosphere with a dawn-dusk asymmetry 2. Parameterization and fitting to observations, *J. Geophys. Res.*, *107*(A8), 1176, doi:10.1029/2001JA000220.

Tsyganenko, N. A., and D. P. Stern (1996), Modeling the global magnetic field of the large-scale Birkeland current systems, *J. Geophys. Res.*, *101*, 27,187–27,198, doi:10.1029/96JA02735.

Turner, D. L., Y. Shprits, M. Hartinger, and V. Angelopoulos (2012), Explaining sudden losses of outer radiation belt electrons during geomagnetic storms, *Nat. Phys.*, *8*, 208–212, doi:10.1038/NPHYS2185.

Weimer, D. R. (2005), Improved ionospheric electrodynamic models and application to calculating Joule heating rates, *J. Geophys. Res.*, *110*, A05306, doi:10.1029/2004JA010884.

Wygant, J. R., et al. (2002), Evidence for kinetic Alfvén waves and parallel electron energization at 4–6 R_E altitudes in the plasma sheet boundary layer, *J. Geophys. Res.*, *107*(A8), 1201, doi:10.1029/2001JA900113.